A Predictive Bandwidth Extended State Observer With Gain Optimization for Model Predictive Speed Control of Electrical Drives

Ruiqi Li, Deqing Huang, *Senior Member, IEEE*, Yong Chen, *Member, IEEE*, and Qiyuan Zhao

***Abstract*—In this study, a predictive bandwidth extended state observer (PB-ESO) with gain optimization is put forward to obtain high dynamic performance and parameters robustness for the model predictive speed control (MPSC) of electrical drives (EDs). The proposed observer preserves the primary feature of standard low bandwidth ESO in terms of strong suppression to measurement noise, while overcoming their main drawbacks, namely the "slow convergence" and "disturbance estimation distortion." First, the conventional ESO-based MPSC scheme is presented, followed by an analysis of the disturbance estimation mechanism of the ESO. Second, the PB, based on the recursive least squares algorithm, is designed to accommodate to the frequency of fast time-varying disturbances in advance. A general mathematical formula for the gain optimization of even-order ESOs is then derived to enhance the estimation accuracy of periodic dynamic interference. In consequence, the gains of PB-ESO are optimized, where stability and fast convergence are ensured rigorously. Finally, a speed control strategy, combining the MPSC scheme and the proposed PB-ESO, is developed in a rational way. Comparative experimental results with existing methods demonstrate the enhanced robustness of the proposed control approach for ED across four representative operating conditions.**

***Index Terms*—Electrical drives (EDs), gains optimization, low bandwidth extended state observer (ESO), model predictive speed control (MPSC), predictive bandwidth.**

I. INTRODUCTION

THE speed control of electrical drives (EDs) is crucial across various industrial and transportation applications, significantly impacting energy efficiency, environmental sustainability, and overall productivity [1], [2]. However, the traditional proportional-integral (PI) speed control strategies struggle to adapt to variable speed conditions and dynamic load variations. Their relatively low convergence rates and limited degrees of freedom hinder optimal performance, especially in high-demand applications where precise speed control is essential. Recently, advancements in microprocessors have facilitated the emergence of model-predictive control (MPC) as a key development in control engineering [3]. Specifically, the model predictive speed control (MPSC) has shown excellent dynamic performance by selecting optimal control laws to minimize speed tracking errors, leading to extensive research and application as a promising method for ED speed control [4].

The MPSC schemes of ED can be categorized into two types, namely finite-control-set model predictive speed control (FCS-MPSC) and continuous-control-set model predictive speed control (CCS-MPSC). The cost function of FCS-MPSC includes both electrical and mechanical states, which complicates the design of appropriate weighting factors necessary for balancing control objectives across different dimensions [5]. In [6], an algebraic design-based FCS-MPSC strategy is proposed to facilitate the selection of weighting factors. In [7], a unified reference voltage is calculated based on the deadbeat concept, eliminating the need for weighting factors. However, this approach remains highly sensitive to parameter variations, as it incorporates both electrical and mechanical parameters, and requires complex multivector modulation schemes to minimize torque harmonics.

CCS-MPSC employs a cascaded architecture where MPC computes torque references for the outer loop controller, while a variety of current controllers and pulsewidth modulation (PWM) strategies can be used in the inner loop [8]. Although CCS-MPSC introduces some delay due to its structure, it generally offers superior global performance without the complications of weight factor design, making it easier to implement.

It is worthy of highlighting that the stability and robustness of MPSC methods mainly depend on the accuracy of predictive model. In situations where inaccuracies arise, techniques for estimating disturbances and uncertainties serve as enhancement tools for ED systems [9], [10]. For instance, in [11] and [12], the Kalman filters are employed for estimating the unknown load, which effectively mitigate the influence of measurement and quantization noise, but the mechanical parameter mismatches

---

Received 20 July 2024; revised 23 September 2024, 28 October 2024, and 4 December 2024; accepted 11 December 2024. Date of publication 16 December 2024; date of current version 28 January 2025. This work was supported in part by the National Natural Science Foundation of China under Grant U21A20169 and Grant 62303383, in part by the Central Government Guides Local Science and Technology Development Project of Sichuan Province under Grant 2024ZYD0018, in part by the Sichuan Science and Technology Program under Grant 2024NSFSC1493, in part by the Sichuan Postdoctoral Research Program under Grant YH1101012372462, and in part by the Fundamental Research Funds for the Central Universities under Grant 2682024CX008. Recommended for publication by Associate Editor A. Safaee. *(Corresponding author: Yong Chen.)*

The authors are with the School of Electrical Engineering, Southwest Jiaotong University, Chengdu 610031, China, and also with the Key Laboratory of Railway Industry of Advanced Energy Traction and Comprehensive Energy Conservation, Southwest Jiaotong University, Chengdu 610031, China (e-mail: liricky@my.swjtu.edu.cn; elehd@home.swjtu.edu.cn; chenyong.sclz@swjtu.edu.cn; 2018117287@my.swjtu.edu.cn).

Color versions of one or more figures in this article are available at https://doi.org/10.1109/TPEL.2024.3518584.

Digital Object Identifier 10.1109/TPEL.2024.3518584

are overlooked. Meanwhile, extended state observers (ESOs) have also been extensively investigated and applied [13], [14], which regard uncertainties and inaccurate parameters as lumped disturbance and extended state [15]. Furthermore, a linear ESO based on the ultralocal model is introduced in [16], eliminating the necessity of parameter involvement in future state predictions. In order to counteract the rapid and time-varying disturbance caused by mismatched parameters, it becomes crucial to enhance the bandwidth of the ESO, which is typically constrained by measurement noise and mechanical system stiffness.

To further improve the robustness of the predictive control system, various enhanced ESOs have been proposed, e.g., the exponential ESO [17], the parallel ESO [18], and the adaptive integral ESO [19]. Besides, the sliding mode observer is also widely regarded as an effective method to overcome perturbation [20], [21].

Notably, all the aforementioned observer techniques utilize the error and the rate of change of error between the current state and the estimated state for estimation, exhibiting time-delay characteristics relative to disturbance. To resolve this, a predictive model error observer (PEMO) is proposed in [22]. However, PEMO primarily focuses on the convergence of the unextended state while neglecting interference estimation performance. This can lead to an excessively high bandwidth setting, making predictive outcomes susceptible to interference from measurement noise. [23] reveals that ESO's interference estimation is essentially a low-pass filtering (LPF) mechanism. Considering that the Chebyshev filter approximates an ideal filter closely, its amplitude-frequency characteristics are utilized for optimizing disturbance estimation of ESO [24]. However, due to gain deviation in the transfer function, it is only applicable to odd-order systems whereas the ED system discussed in this paper belongs to even-order systems. Furthermore, even with optimized ESO gain values, fixed-bandwidth designs can still pose challenges when balancing noise suppression and convergence.

An alternative approach to bolster system robustness involves parameter identification. In [25], an adaptive ESO (AESO) with parameter identification is introduced in active disturbance rejection control, which is capable of simultaneously identifying multiple mechanical parameters. Furthermore, an LPF and a low control gain are employed to suppress the measurement noise in the speed feedback loop, thereby achieving precise parameter identification. Nevertheless, this modification degrades the convergence rate of parameter identification and the dynamic performance in suppressing the time-varying disturbance rapidly. Besides, it exclusively focuses on the outcomes of parameter identification while neglecting an exploration of overall motor control performance. In essence, existing parameter identification strategies address system model mismatches but fail to account for unknown disturbances or unmodeled dynamics, a limitation prevalent in broader parameter identification research [26], [27], [28].

To optimize the tradeoff between noise suppression and rapid convergence, while mitigating amplitude fluctuations in disturbance estimation, this paper proposes a predictive bandwidth ESO (PB-ESO) with gain optimization. This method aims to improve both the dynamic performance and parameter robustness of CCS-MPSC in EDs.

The main contributions can be described as follows.

1) A PB-ESO based on the recursive least squares (RLS) algorithm is proposed. For step interference caused by model mismatch and sudden load changes, it can adjust the bandwidth in advance to adapt to the ultra-high-frequency variations of the interference and quickly converge to the steady state. In addition, for interference with frequency changes within the bandwidth, it switches to a low-bandwidth ESO. Since this process is transient, no high-frequency noise is introduced into the estimated state.
2) A general formula for gain optimization in even-order ESO systems is derived and combined with PB-ESO. The combination of these two methods is mutually beneficial. Gain optimization enhances the disturbance estimation accuracy of ESO within the bandwidth. The variable bandwidth of PB-ESO provides greater flexibility to the gain-optimized general formula. In other words, it can reduce the maximum fluctuation of the estimated interference to a small range without needing to focus on the roll-off speed of the ESO transition zone.
3) Based on the PB-ESO with gain optimization, the MPSC of ED is developed and evaluated to enhance dynamic performance and parameter robustness under conditions such as inertia mismatch, abrupt load changes, dynamic reference signals, and high-frequency periodic loads.

The rest of this article is organized as follows. In Section II, the conventional CCS-MPSC method based on ESO is described. Section III proposes a CCS-MPSC method based on a PB-ESO with gain optimization, denoted by MPSC-PB-ESO. In Section IV, the experimental results are presented and analyzed. Finally, Section V concludes this article.

II. PRELIMINARIES

A. Mechanical Dynamic Model of ED

The mechanical dynamic model of the permanent magnet synchronous motor (PMSM) and the induction motor (IM) commonly used in ED is described as follows [29]:

$$J\dot{\Omega} = T_e - B\Omega - T_L - T_c\,\mathrm{sign}(\Omega) \tag{1}$$

where Ω is the rotor angular speed of ED, J is the moment of inertia, B and T_c are the coefficients of viscous and coulomb friction torque, respectively, and T_e and T_L represent the electromagnetic and load torques of the drive model.

In practical systems, the discrepancies may arise between the actual parameters of the drive model and those set in (1) due to load disturbances and temperature variations, leading to model mismatch. To overcome this, the ultralocal model (2) is presented by combining load torque and inaccuracy mechanical parameter loads to the lump load T_f, which is expressed as follows:

$$\begin{cases} J_0\dot{\Omega} = T_e - T_f \\ \dot{T}_f = g \end{cases} \tag{2}$$

where g denotes the change rate of lump load. Defining ΔJ, ΔB, ΔT_c as the perturbed values and J_0, B_0, T_{c0} as the initial values of model parameters in (1), the lump load T_f is defined as follows:

$$T_f = [(B_0 + \Delta B)\Omega + (T_{c0} + \Delta T_c)\,\mathrm{sign}(\Omega) + T_L] + \Delta J\dot{\Omega}. \tag{3}$$

B. Conventional CCS-MPSC Based on ESO

Based on the ultralocal model (2), an ESO is presented to estimate the lump disturbance as follows [25]:

$$\begin{cases} \hat{e} = \hat{\Omega} - \Omega - \zeta_1 \\ \dot{\hat{\Omega}} = \frac{1}{J_0}T_{e0} - \hat{\delta} - \beta_1\hat{e} \\ \dot{\hat{\delta}} = \beta_2\hat{e} \end{cases} \tag{4}$$

where $\hat{\Omega}$ is the estimated angular speed, ζ_1 the measurement noise in the speed sensor, $\hat{e}$ the estimated error of angular speed, $\hat{\delta}$ the estimated lump disturbance, T_{e0} the input of ESO, and β_1, β_2 are the gains of ESO.

Due to mismatch in the torque model $\Delta T_e = T_e - T_{e0}$ and measurement noise ζ_2 in the current sensor, the lump disturbance is expressed as follows:

$$\delta = \frac{1}{J_0}(T_f + \zeta_2 - \Delta T_e). \tag{5}$$

By adopting a normal Euler forward method to the second equation in (4), the one-step predictive model of the motor's speed is

$$\hat{\Omega}(k+1) = \hat{\Omega}(k) + T_{\mathrm{sp}}\left(\frac{1}{J_0}T_{e0}(k) - \hat{\delta}(k) - \beta_1\hat{e}(k)\right) \tag{6}$$

where T_{sp} is the sampling period.

The cost function is designed as follows:

$$J_c = [\Omega^* - \hat{\Omega}(k+1)]^2 \tag{7}$$

where Ω^* is the reference speed. By solving $\partial J_c/\partial T_{e0}(k) = 0$, the optimal reference torque of CCS-MPSC is then derived as [29]

$$T_e^* = \frac{J_0(\Omega^* - \hat{\Omega}(k))}{T_{\mathrm{sp}}} + J_0\hat{\delta}(k) + J_0\beta_1\hat{e}(k) \tag{8}$$

where $(T_e^*)^2 \le (T_{e,\mathrm{lim}})^2$, and $T_{e,\mathrm{lim}}$ represents the maximum torque, which accounts for the physical constraints of ED systems. The reference torque T_e^* can be tracked by the inner current loop (CL) controller.

C. Disturbance and Noise Analysis

From (8), it is well known that inaccurate interference observations would generate a negative impact on the speed tracking performance. Therefore, a study on disturbance and noise is essential and beneficial for designing an improved control method of CCS-MPSC.

Combining (2) and (4), the estimated error dynamic equation is given as

$$\dot{\hat{e}} = \dot{\hat{\Omega}} - \dot{\Omega} - \dot{\zeta}_1 = \delta - \hat{\delta} - \beta_1\hat{e} - \dot{\zeta}_1 \tag{9}$$

where the relationship $\delta = (T_f + \zeta_2 - \Delta T_e)/J_0$ is used. Taking the Laplace transformation for (9) and noticing from the third equation of (4) that $\hat{\delta}(s) = \beta_2\hat{e}(s)/s$, it has

$$s\hat{e}(s) = \delta(s) - \frac{1}{s}\beta_2\hat{e}(s) - \beta_1\hat{e}(s) - s\zeta_1(s). \tag{10}$$

By simplifying (10), the estimated error dynamic equation in the s-domain is

$$\hat{e}(s) = \frac{s}{s^2 + \beta_1 s + \beta_2}\delta(s) - \frac{s^2}{s^2 + \beta_1 s + \beta_2}\zeta_1(s). \tag{11}$$

Noticing the definition of estimation error $\hat{e}$ in (4), it follows from (11) that

$$\hat{\Omega}(s) - \Omega(s) = \frac{s}{s^2 + \beta_1 s + \beta_2}\delta(s) + \frac{\beta_1 s + \beta_2}{s^2 + \beta_1 s + \beta_2}\zeta_1(s). \tag{12}$$

To guarantee the stability of ESO, the gains of ESO based on pole assignment method are designed as:

$$\begin{cases} \beta_1 = 2\omega_o \\ \beta_2 = \omega_o^2 \end{cases} \tag{13}$$

where $\omega_o > 0$ represents the bandwidth of ESO. Substituting (13) into (12), we have

$$\hat{\Omega}(s) - \Omega(s) = \frac{s}{s^2 + 2\omega_o s + \omega_o^2}\delta(s) + \frac{2\omega_o s + \omega_o^2}{s^2 + 2\omega_o s + \omega_o^2}\zeta_1(s). \tag{14}$$

The characteristic polynomial of (14) is given by $s^2 + 2\omega_o s + \omega_o^2$, implying that the estimated angular speed $\hat{\Omega}$ will converge to its actual value when the lump disturbance δ remains constant or change slowly. Moreover, the measurement noise ζ_1 can be effectively suppressed in the estimated speed.

Based on (11) and $\hat{\delta}(s) = \beta_2\hat{e}(s)/s$, the transfer function between the estimated lumped disturbance $\hat{\delta}$ and the actual lumped disturbance δ is then derived as follows:

$$\hat{\delta}(s) = \frac{\beta_2}{s^2 + \beta_1 s + \beta_2}\delta(s) - \frac{\beta_2 s}{s^2 + \beta_1 s + \beta_2}\zeta_1(s). \tag{15}$$

Noticing (5) and (13), (15) is rewritten as

$$\hat{\delta}(s) = \left(\frac{\omega_o}{s + \omega_o}\right)^2\left[\frac{1}{J_0}(T_f(s) + \zeta_2(s) - \Delta T_e(s))\right] - \frac{\omega_o^2 s}{s^2 + 2\omega_o s + \omega_o^2}\zeta_1(s). \tag{16}$$

From the term $(\omega_o/(s + \omega_o))^2$ on the right-hand side of (16), it is evident that the lumped disturbance estimation mechanism of the ESO can be interpreted as a Butterworth LPF, where the ESO bandwidth ω_o corresponds to the LPF's cutoff frequency. The estimated disturbance will converge to its actual value when the frequency of the lumped disturbance δ is within the bandwidth ω_o. In addition, the high-frequency noise ζ_2 outside the bandwidth can be filtered out.

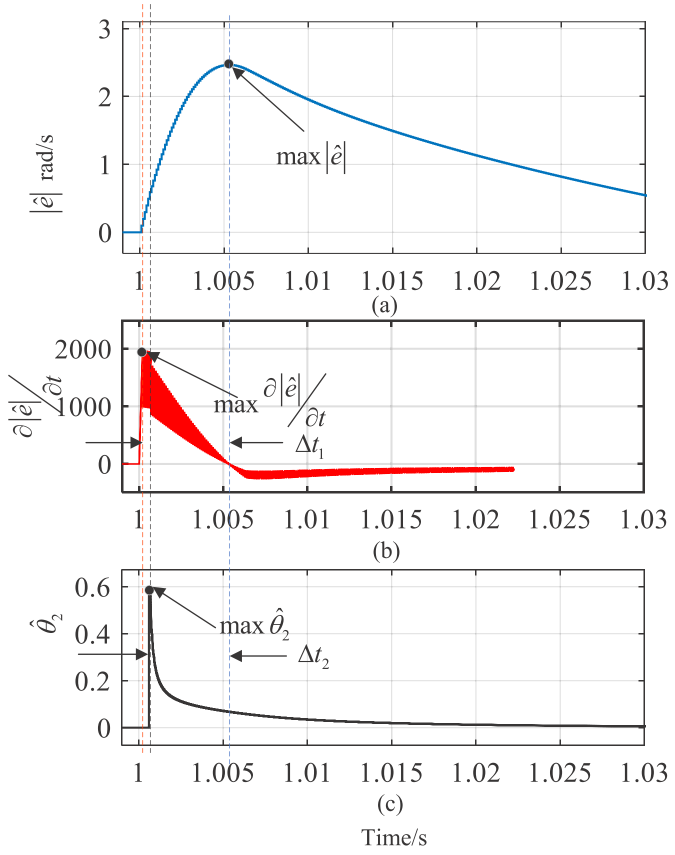

Fig. 1. Dynamic process of the estimation error under the step change of disturbance. (a) Estimation error of ESO. (b) Differentiation of the estimation error. (c) Dynamic fitting process of RLS.

In fact, as demonstrated in (3) and (5), the lumped disturbances acting on the drive system can exhibit multiple orders and change rapidly during dynamic speed tracking or sudden load variations. If the bandwidth ω_o of ESO is insufficient, the estimated disturbance $\hat{\delta}$ and speed $\hat{\Omega}$ will be distorted. Consequently, the optimal control law T_e^* derived from (8) will be inaccurate, leading to oscillations of the MPSC system at the reference point and potential system instability. Although increasing the bandwidth ω_o of the ESO can improve the dynamics of the observer, it also introduces high-frequency measurement noise ζ_2 into the control loop.

To select the appropriate bandwidth of ESO that balance noise suppression and convergence, several AESOs have been proposed [30], [31]. However, with step changes in parameters and disturbances, these methods remain passive due to the delay caused by the maximum disturbance [22].

Consequently, the suitability of these observers should be further enhanced to improve the overall performance of the CCS-MPSC system under various conditions.

III. PB-ESO-BASED MODEL PREDICTIVE SPEED CONTROL WITH GAIN OPTIMIZATION

To address the aforementioned issues, we propose a PB-ESO with gain optimization, which is then integrated into the CCS-MPSC system of ED to enhance the overall control performance.

A. PB-ESO Design With Gain Optimization

1) Design of PB: From (14) and (16), it is clear that the bandwidth determines the performance of the ESO. However, due to the random and highly nonlinear nature of motor parameter variations and disturbances, it is difficult to accurately determine the system's frequency for selecting an optimal bandwidth. To address this challenge, a PB with adaptive and proactive disturbance suppression capabilities is proposed.

Fig. 1(a) illustrates the speed estimation error dynamic process of the ESO under the step disturbance caused by model mismatches at 1s. Due to the influence of inertia elements such as the motor rotor, inductance, and filters, the estimation error gradually changes and exhibits convex behavior. This demonstrates that the error-based adaptive bandwidth has a significant time delay compared to the actual disturbance's frequency.

Fig. 1(b) illustrates the rate of change of the estimation error under model mismatches. This rate peaks Δt_1 s before the estimation error itself, resembling an approximate step signal. This behavior suggests that feeding $\partial|\hat{e}|/\partial t$ into the ESO's bandwidth could synchronize the bandwidth adjustment with the disturbance.

However, due to the presence of ripples in the speed estimation error, the rate of error variation $\partial|\hat{e}|/\partial t$ exhibits oscillations. To prevent this, a linear fitting model based on the RLS algorithm is used to smooth the rate. The execution steps of the RLS algorithm are summarized as follows [22], [32]:

$$\begin{cases} \mathbf{P}(k) = \mathbf{P}(k-1) - \frac{\mathbf{P}(k-1)\bar{\mathbf{x}}(k)\bar{\mathbf{x}}^T(k)\mathbf{P}(k-1)}{I+\bar{\mathbf{x}}^T(k)\mathbf{P}(k-1)\bar{\mathbf{x}}(k)} \\ \hat{\boldsymbol{\theta}}(k) = \hat{\boldsymbol{\theta}}(k-1) + \mathbf{P}(k)\bar{\mathbf{x}}(k)[\bar{y}(k) - \bar{\mathbf{x}}^T(k)\hat{\boldsymbol{\theta}}(k-1)] \end{cases} \tag{17}$$

where $\bar{\mathbf{x}} = [1, n_k]^T$, n_k represents the number of sampling period, $\bar{y} = |\hat{e}|$ is the absolute value of estimated speed error, $\mathbf{P}(k)$ is the gain matrix, and $\hat{\boldsymbol{\theta}}(k) = [\hat{\theta}_1, \hat{\theta}_2]^T$ is the estimated parameters of linear equation: $\mathbf{Y} = \mathbf{X}\hat{\boldsymbol{\theta}}(k)$, $\mathbf{Y} = [y(1), y(2), y(3)\ldots y(k)]^T$, $y(k) = \bar{\mathbf{x}}(k)^T\hat{\boldsymbol{\theta}}(k)$ and $\mathbf{X} = [\bar{\mathbf{x}}(1), \bar{\mathbf{x}}(2), \bar{\mathbf{x}}(3)\ldots\bar{\mathbf{x}}(k)]$.

The number of sampling period n_k is calculated by

$$\begin{cases} n_k = \frac{\boldsymbol{\tau}}{T_{\text{sp}}}, & |\hat{e}| > e_{\text{stable}} \\ n_k = 0, & \text{Otherwise} \end{cases} \tag{18}$$

where $\boldsymbol{\tau}$ is the timer value after activation, and e_{stable} denotes the steady-state speed estimation error. The timer activates only when the system experiences disturbances, ensuring that steady-state ripple does not interfere with the RLS algorithm.

Fig. 1(c) illustrates the dynamic fitting of the estimation error using the RLS algorithm. The parameter $\hat{\theta}_2$ exhibits behavior similar to the rate of change $\partial|\hat{e}|/\partial t$ but with significantly improved smoothness. Thus, $\hat{\theta}_2$ can be fed into the ESO bandwidth, allowing it to adapt effectively to rapidly changing disturbances.

The PB is then designed as

$$\omega_p = [a\hat{\theta}_2\omega_o + 1]\omega_o \tag{19}$$

where $a \geq 1$ is a scaling coefficient, and ω_o is the initial bandwidth. From Fig. 1(c), when disturbances are weak, the value of $\hat{\theta}_2$ may fall below 1. The coefficient a can amplify changes in $\hat{\theta}_2$, ensuring that the PB ω_p can quickly adjust to required level.

Subsequently, the PB-ESO is derived, sharing the same expression as (4) but with different gains ($\beta_1 = 2\omega_p$, $\beta_2 = \omega_p^2$).

When the interference changes slowly, $\hat{\theta}_2 \to 0$ and $\omega_p \to \omega_o$. In this case, the PB-ESO reverts to a conventional low-bandwidth ESO, effectively tracking slow-varying disturbances and suppressing high frequency measurement noise. When the observation system is disrupted, the variable $\hat{\theta}_2$ is influenced, and ω_p follows the relationship $\omega_p \to a\hat{\theta}_2\omega_o^2 + \omega_o$.

As shown in Fig. 1(c), due to the sensitivity of $\hat{\theta}_2$ to disturbances, the PB ω_p rises to its peak with a rate resembling a step signal, ensuring that the ESO has sufficient bandwidth to estimate step disturbances accurately. Given the transient nature of this bandwidth adjustment—lasting only a few microseconds—high-frequency noise lacks sufficient time to enter the observation system. This mechanism achieves a balance between rapid convergence and effective noise suppression.

2) Parameter Tuning of Even-Order ESO: The design of the PB-ESO improves the system's capability to manage fast time-varying disturbances under noise constraints. However, the disturbance estimation performance is limited by the amplitude attenuation inherent to the Butterworth LPF. To enhance speed tracking and disturbance estimation, the ESO parameters should be further optimized with ideal filters that maintain a unity magnitude response within the bandwidth.

The Chebyshev filter, resembling an ideal filter, is chosen to optimize the ESO's gain. The characteristics of the N-order Chebyshev Type-I filter are given by

$$|H(j\omega)| = \sqrt{\frac{1}{1 + \varepsilon^2 \cdot T_N^2\left(\frac{\omega}{\omega_c}\right)}} \tag{20}$$

where ω_c is the cutoff frequency corresponding to the bandwidth of ESO, ε is the ripple coefficient of pass band, and $T_N\left(\frac{\omega}{\omega_c}\right)$ is an N-order Chebyshev polynomial defined as

$$T_N = \begin{cases} \cos\left[N\cos^{-1}\left(\frac{\omega}{\omega_c}\right)\right], & \left|\frac{\omega}{\omega_c}\right| \leq 1 \\ \cosh\left[N\cosh^{-1}\left(\frac{\omega}{\omega_c}\right)\right], & \left|\frac{\omega}{\omega_c}\right| > 1. \end{cases} \tag{21}$$

The passband ripple coefficient ε can be determined by the maximum amplitude fluctuation γ in the passband. For $|\frac{\omega}{\omega_c}| \leq 1$, with $0 \leq T_N^2\left(\frac{\omega}{\omega_c}\right) \leq 1$, $H(j\omega)$ will fluctuate between unity and $1/\sqrt{1+\varepsilon^2}$. Thus, γ is given by

$$\gamma = 20\lg 1 - 20\lg\frac{1}{\sqrt{1+\varepsilon^2}} = -20\lg\frac{1}{\sqrt{1+\varepsilon^2}} \tag{22}$$

where γ primarily determines the attenuation speed at cut-off frequency ω_c and the fluctuation level in the passband. Although increasing γ will reduce the amplitude-frequency gain in the transitional band, it will cause larger amplitude-frequency fluctuations in the passband.

From (20), and let $\omega \to -js$, we have

$$H(s)H(-s) = |H(j\omega)|^2_{s=j\omega} = \frac{1}{1 + \varepsilon^2 \cdot T_N^2\left(\frac{-js}{\omega_c}\right)}. \tag{23}$$

By setting

$$1 + \varepsilon^2 \cdot T_N^2\left(\frac{-js}{\omega_c}\right) = 0 \tag{24}$$

the $2N$ poles of (23) can be calculated accordingly, where half of them belong to $H(s)$ and half to $H(-s)$. To ensure the stability, the poles in the left half-plane of the s-plane should be assigned to $H(s)$. Then, the transfer function of the Chebyshev filter is obtained by

$$H(s) = \frac{K}{\prod_{k=1}^{N}(s - s_k)} \tag{25}$$

where s_k represents the kth pole of (23) determined by (24), and K the gain of the transfer function $H(s)$. Substituting $\omega = 0$ rad/s into (20) and (25), then

$$|H(0)| = \sqrt{\frac{1}{1 + \varepsilon^2 \cdot T_N^2\left(\frac{0}{\omega_c}\right)}} = \frac{K}{\prod_{k=1}^{N}(0 - s_k)}. \tag{26}$$

Combining (21) and (26), the gain K is derived as

$$K = \begin{cases} \prod_{k=1}^{N} s_k, \ \text{if} \ \ N \ \ \text{is} \ \ \text{odd}, \\ (-1)^N\sqrt{\frac{1}{1+\varepsilon^2}}\prod_{k=1}^{N} s_k, \ \text{if} \ \ N \ \ \text{is} \ \ \text{even}. \end{cases} \tag{27}$$

The transfer function of the disturbance estimation of the N-order ESO can be written as [23]

$$G(s) = \frac{\beta_N}{\prod_{k=1}^{N}(s - p_k)} = \frac{\beta_N}{\left(s^n + \sum_{i=1}^{N-1}\beta_i s^{n-i+1} + \beta_N\right)} \tag{28}$$

where p_k is the kth pole of N-order ESO, β_i is the ith parameter, and β_N is the Nth parameter satisfying $\beta_N = (-1)^N\prod_{k=1}^{N} p_k$.

Comparing (26) and (28), if we set the poles of $G(s)$ equal to the poles of $H(s)$, then $\beta_N = K$ for an odd-order ESO. This indicates that the gains of an odd-order ESO can be uniquely determined by the Chebyshev filter.

For an even-order ESO, if we set the poles of $G(s)$ and $H(s)$ to be the same, $K = (-1)^N\sqrt{\frac{1}{1+\varepsilon^2}}\prod_{k=1}^{N} s_k \neq (-1)^N\prod_{k=1}^{N} p_k$. In this case, the magnitude frequency response for even-order ESO with gain optimization is derived as

$$|G(j\omega)| = \sqrt{\frac{1+\varepsilon^2}{1 + \varepsilon^2 \cdot T_N^2\left(\frac{\omega}{\omega_c}\right)}}. \tag{29}$$

For $|\frac{\omega}{\omega_c}| \leq 1$, $0 \leq T_N^2\left(\frac{\omega}{\omega_c}\right) \leq 1$, $|G(j\omega)|$ will fluctuate between unity and $\sqrt{1+\varepsilon^2}$. Thus, the maximum amplitude fluctuation γ_1 for an optimized even-order ESO is

$$\gamma_1 = 20\lg\sqrt{1+\varepsilon^2} - 20\lg 1 = 20\lg\sqrt{1+\varepsilon^2}. \tag{30}$$

Fig. 2 presents the Bode diagram of the conventional ESO and the gain-optimized ESO with varying values of γ_1, both set to a bandwidth of 100 rad/s. The gain-optimized ESO

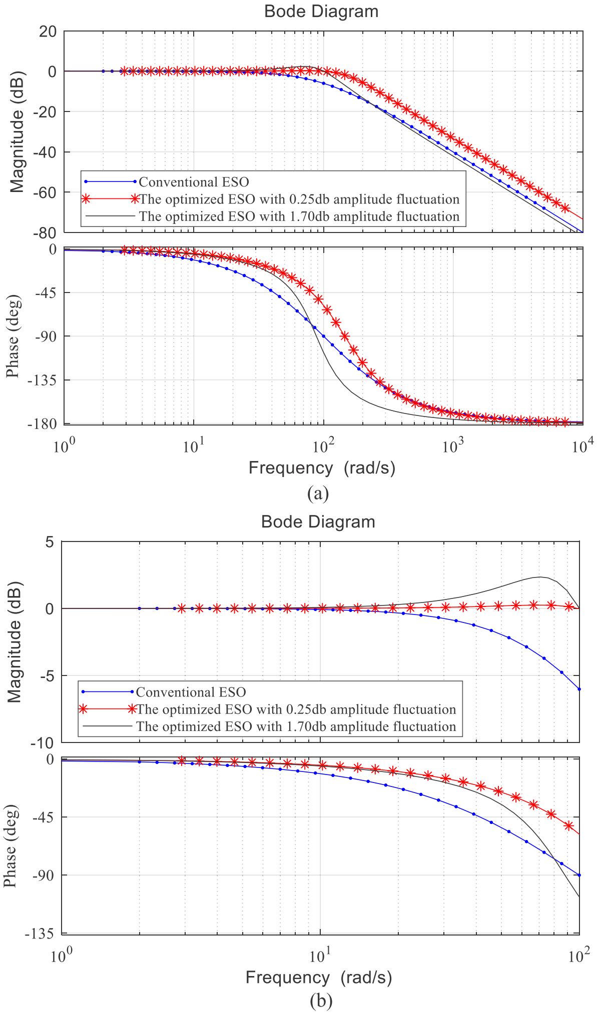

Fig. 2. Bode plot comparison among the conventional ESO, the optimized ESO with 0.25 dB amplitude fluctuation range and the optimized ESO with 1.70 dB amplitude fluctuation range. (a) Original plot, (b) Zoom area in 1–100 rad/s.

maintains a closer proximity to 0dB compared to the conventional ESO, though it does not achieve the same degree of flatness.

Notably, adjusting the parameter γ_1 can reduce amplitude fluctuations of the observer but also lowers the roll-off rate in the transition zone, thereby diminishing the suppression capability for high-frequency noise. Consequently, while the gain-optimized ESO outperforms the conventional ESO in disturbance estimation, determining an optimal value for γ_1 remains a challenge.

3) PB-ESO With Optimized Gains: Considering the flexibility and sensibility of PB mentioned in Section III-A1 for actual disturbances frequency, it is naturally employed to decouple the suppression of high-frequency noise from the desired observation performance.

To facilitate the design, we first ignore measurement noise in the mechanical system of the ED and its disturbance observer (4). The transfer function of disturbance estimation can be rewritten as:

$$\hat{\delta}(s) = \frac{\beta_2}{s^2+\beta_1 s+\beta_2}\delta(s) = G(s)\delta(s). \tag{31}$$

Referring to Section III-A2, and assuming a maximum amplitude fluctuation range γ_1 to be 0.25 dB (a small fluctuation range), we have $\varepsilon \approx 0.243$.

Setting $|G(j\omega)| = \sqrt{G(j\omega)G(-j\omega)}$ and substituting $\omega \rightarrow -js$ with $N = 2$, we get

$$G(j\omega)G(-j\omega) = \frac{1.059}{1+0.059\cdot T_2^2\left(\frac{\omega}{\omega_p}\right)}. \tag{32}$$

Here, the PB ω_p replaces the fixed cut-off frequency.

The poles of (32) are given by

$$T_N\left(\frac{-js}{\omega_p}\right) = \pm j\sqrt{17}. \tag{33}$$

Using the relationship (21) and noting $N = 2$, we have the following Chebyshev polynomial for (33):

$$T_2\left(\frac{-js}{\omega_p}\right) = 2\left(\frac{-js}{\omega_p}\right)^2 - 1 = \pm j\sqrt{17}. \tag{34}$$

The polynomial (34) has four poles, with half belong to $G(s)$ and the other half to $G(-s)$. To ensure system stability, the poles in the left half-plane of the s-plane should be assigned to $G(s)$. Thus, the poles of $G(s)$ are derived as

$$p_1 = (-0.9+1.145i)\omega_p,\ \ p_2 = (-0.9-1.145i)\omega_p. \tag{35}$$

Using these poles, the transfer function of PB-ESO with gain optimization is obtained as follows:

$$G(s) = \frac{2.121\omega_p^2}{s^2+1.801\omega_p s+2.121\omega_p^2}. \tag{36}$$

By comparing (31) with (36), the optimized gains of PB-ESO are determined as follows:

$$\beta_1 = 1.801\omega_p,\ \ \beta_2 = 2.121\omega_p^2. \tag{37}$$

4) Stability and Convergence Analysis: Equation (35) shows that the poles of the characteristic polynomial of the PB-ESO, when subjected to the gain optimization, are all situated in the left half-plane. This confirms the stability of the proposed observer.

Rewriting the PB of (19), its form changes to the following:

$$\omega_p = [a\hat{\theta}_2\omega_o + 1]\omega_o = l\omega_o \tag{38}$$

where $l \geq 1$.

Substituting (38) into (35), the poles of the proposed ESO become

$$p_1 = (-0.9+1.145i)l\omega_o,\ \ p_2 = (-0.9-1.145i)l\omega_o. \tag{39}$$

The convergence rate is primarily governed by the real part of system's poles, where a smaller real part corresponds to a faster dynamic response. For the proposed observer, the real parts of the poles are all equal to $-0.9l\omega_o$. With $l \gg 1$ during the dynamic process, the proposed ESO achieves a higher convergence rate than the conventional ESO. In addition, due to the transient characteristics of the PB, even with amplified observer

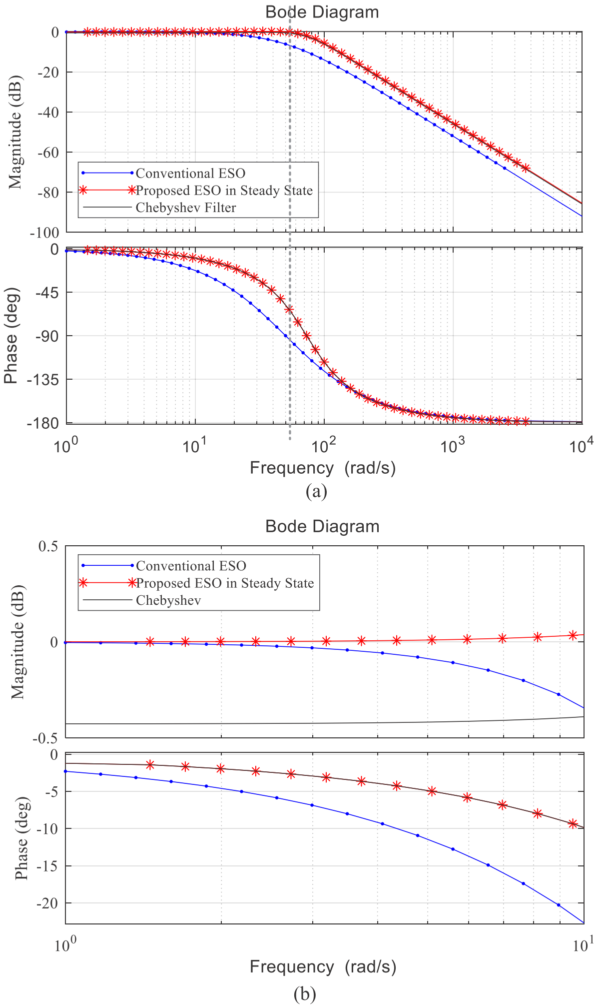

(a)

(b)

Fig. 3. Bode plot comparison among the proposed ESO in steady state, the conventional ESO, and the Chebyshev filter. (a) Original plot, (b) Zoom area in 1–10 rad/s.

gains, high-frequency noise interference is not introduced into the observation system.

In steady-state conditions, the variable $\hat{\theta}_2$ approaches to zero causing the PB ω_p to converges to the low-bandwidth ω_o. Setting $\omega_o = 50$ rad/s, Fig. 3 compares the steady-state observation performance of the proposed observer with that of the conventional ESO and the Chebyshev filter. The results show that the proposed observer provides a higher gain in the passband and is closer to 0 dB with minimal amplitude fluctuation.

B. CCS-MPSC Based on Proposed Observer

Now, recalling the proposed PB-ESO with gain optimization in Section III-A, its final expression is

$$\begin{cases} \hat{e} = \hat{\Omega} - \Omega \\ \dot{\hat{\Omega}} = \frac{1}{J_0} T_{e0} - \hat{\delta} - \beta_1 \hat{e} \\ \dot{\hat{\delta}} = \beta_2 \hat{e} \end{cases} \tag{40}$$

where $\beta_1 = 1.801\omega_p$, $\beta_2 = 2.121\omega_p^2$. Considering (6) and (8), the PB-ESO with gain optimization is then integrated into the CCS-MPSC of ED system to enhance the speed tracking performance and robustness.

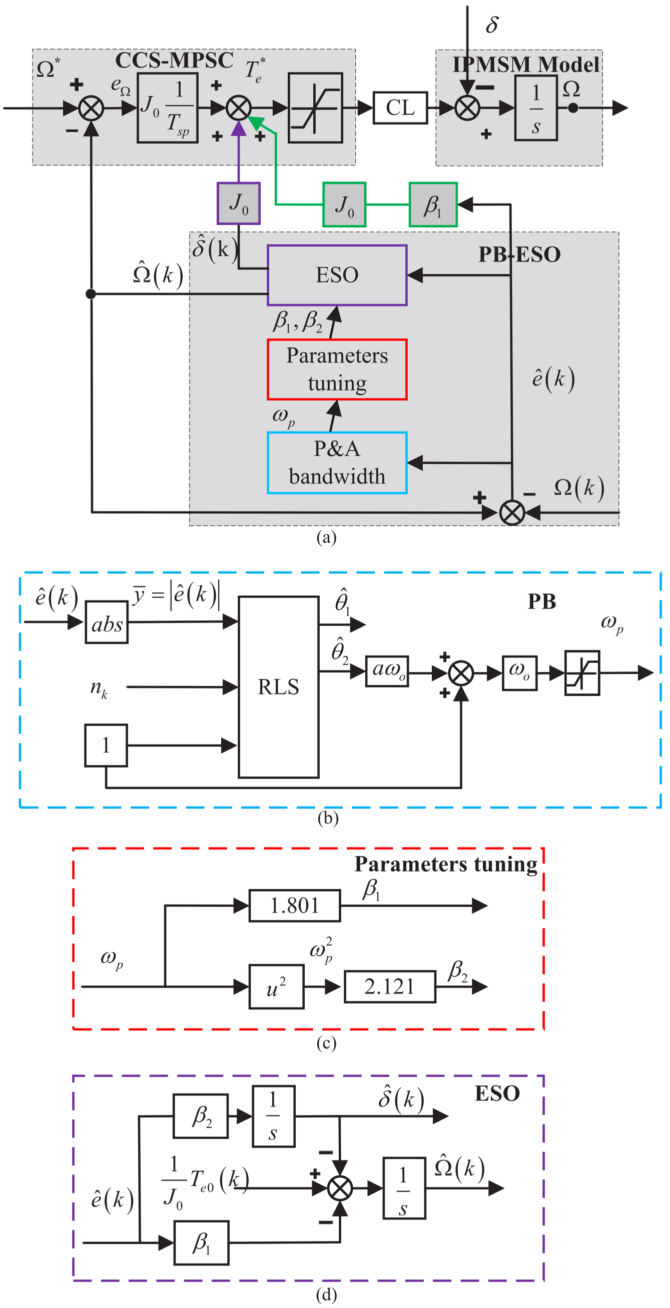

(a)

(b)

(c)

(d)

Fig. 4. PB-ESO based CCS-MPSC controller. (a) General architecture. (b) PB. (c) Parameters tuning. (d) ESO.

The block diagram for the proposed MPSC-PB-ESO is depicted in Fig. 4, where CL denotes the CL. Fig. 4(b)–(d) depicts the block diagrams of PB module, parameters module, and ESO module, respectively.

The optimal control law (8) is updated in real time using the estimated angular speed $\hat{\Omega}$ and lump disturbance $\hat{\delta}$ of the proposed observer. Once the reference torque T_e^* is obtained, an current controller is employed to ensure that the motor generates the desired torque. Fig. 5 presents the overall block diagram of MPSC-PB-ESO.

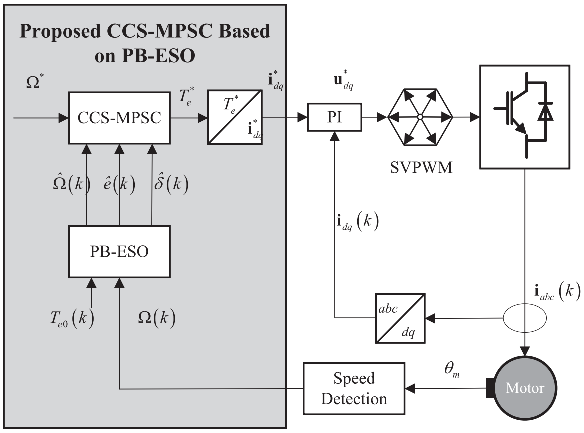

Fig. 5. Block diagram of the motor control system.

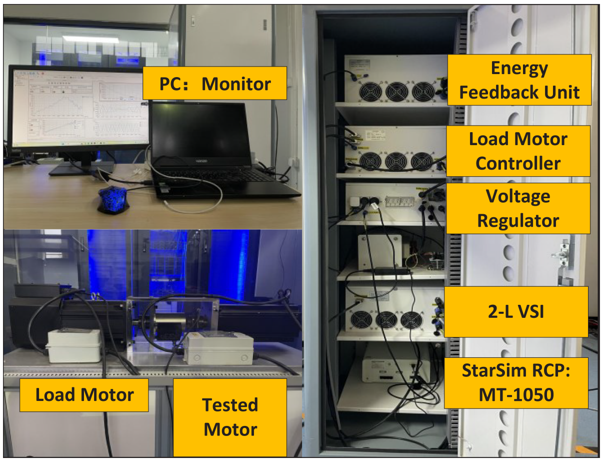

Fig. 6. IPMSM test platform.

TABLE I
SPECIFICATION OF THE IPMSM

Parameters	value
Rated Power P_n	2.3 kW
Rated speed Ω_n	1500 r/min
Rated torque T_n	$14.6\ \mathrm{N\cdot m}$
Rated voltage U_n	220 V
Rated current I_n	7.5 A
d-axis inductance L_d	2.05741 mH
q-axis inductance L_q	3.97058 mH
Pole pairs n_p	4
Rotor flux ψ_f	0.2858 Wb
Rotational inertia J	$0.009\ \mathrm{kg\cdot m^2}$
Encoder	2500 pulses per revolution
DC link voltage V_{dc}	311 V
PWM frequency f_s	10 kHz
sampling periods T_{sp}	0.001 s

IV. EXPERIMENTAL RESULTS

To evaluate the effectiveness of the proposed method, the experiments were performed on an interior PMSM (IPMSM) test platform, as illustrated in Fig. 6. The setup includes a 2.3 kW IPMSM, a 3 kW IM, a control cabinet featuring a two-level voltage source inverter integrated with a rapid control prototype controller, a personal computer for data monitoring, and a photoelectric rotary encoder. The detailed specifications of the experimental setup are presented in Table I.

The experiments compare the proposed MPSC-PB-ESO with the PEMO-based CCS-MPSC (MPSC-PEMO) and traditional ESO-based CCS-MPSC (MPSC-ESO) methods under various conditions, focusing on the robustness and dynamic tracking performance of the system. Table II provides the parameter settings for the three methods.

In the MPSC-ESO method, two bandwidths are used: 50 rad/s and 250 rad/s. The method with a bandwidth of 50 rad/s is labeled MPSC-ESO1, and the one with a bandwidth of 250 rad/s is labeled MPSC-ESO2. These settings are used to demonstrate the impact of varying bandwidths on control system performance and observation accuracy.

For the PEMO method, the bandwidth is set to be 50 rad/s, and the predictive step m is set to be 50 to avoid potential system instability with higher values. In the PB-ESO method, the base bandwidth ω_o is fixed at 50 rad/s, the maximum bandwidth is set to be 250 rad/s, and the coefficient a is set to 10.

For fair comparison, the identical PI current controller (d-axis parameter: $k_{\mathrm{Pid}} = 2.255$, $k_{\mathrm{Iid}} = 660$, q-axis parameter: $k_{\mathrm{Piq}} = 4.367$, $k_{\mathrm{Iiq}} = 660$) and the space vector pulsewidth modulation (SVPWM) technology are employed in the inner CL of ED systems [33]. It is important to note that, as the primary focus of this article is on speed control in ED, the control performance of the current is not specifically highlighted.

All methods are implemented and executed within a sampling period of 100 μs on the Xilinx FPGA-XC7Z100 (CPU: 800 MHz) for comparison. Table III presents the maximum execution time of each algorithm throughout the entire operational phase. Specifically, the execution times of MPSC-PB-ESO and MPSC-PEMO are identical at 35 μs, representing a slight increase of 5 μs compared to MPSC-ESO, which is attributed to the execution of the RLS algorithm.

A. Speed Performance Under Rated Conditions

In this section, the performance of the proposed method and the comparison methods are evaluated under rated conditions. Fig. 7 shows the dynamic and steady-state responses from 0 to the rated speed of 1500 r/min under the rated load for different methods. Each part of Fig. 7 contains three subplots: the first displays the speed tracking performance, the second shows the q-axis current reference (red line) alongside its actual value (blue line), and the third illustrates the load disturbance estimation performance.

As shown in Fig. 7, MPSC-ESO1 reaches the rated speed of 1500 r/min under the rated load in 5.5 s, while MPSC-ESO2, MPSC-PEMO, and MPSC-PB-ESO achieve the same speed within 3.6 s. Once the motor reaches steady state, the ripple in the MPSC-ESO2 method is larger than that of the other methods, reaching about 20 r/min, whereas the ripple in other methods remains below 1.4 r/min. This highlights a limitation of conventional fixed-bandwidth ESO, which struggles to achieve an optimal balance between response time and ripple suppression. In contrast, both the MPSC-PEMO and MPSC-PB-ESO methods offer better compromises between these two factors.

Moreover, all methods effectively track the q-axis reference using a PI controller with identical parameters. However,

TABLE II
THE PARAMETERS OF DIFFERENT OBSERVERS

Parameters	MPSC-ESO1	MPSC-ESO2	MPSC-PEMO	MPSC-PB-ESO
Bandwidth	$\omega_o = 50$ rad/s	$\omega_o = 250$ rad/s	$\omega_o = 50$ rad/s	$\omega_o = 50$ rad/s , $\omega_{\max} = 250$ rad/s
Gains	$\beta_1 = 100, \beta_2 = 2500$	$\beta_1 = 500, \beta_2 = 62500$	$\beta_1 = 100, \beta_2 = 2500$	$\beta_1 = 1.801\omega_p, \beta_2 = 2.121\omega_p^2$
Predictive steps	/	/	$m = 50$	/
The coefficient a	/	/	/	$a = 10$

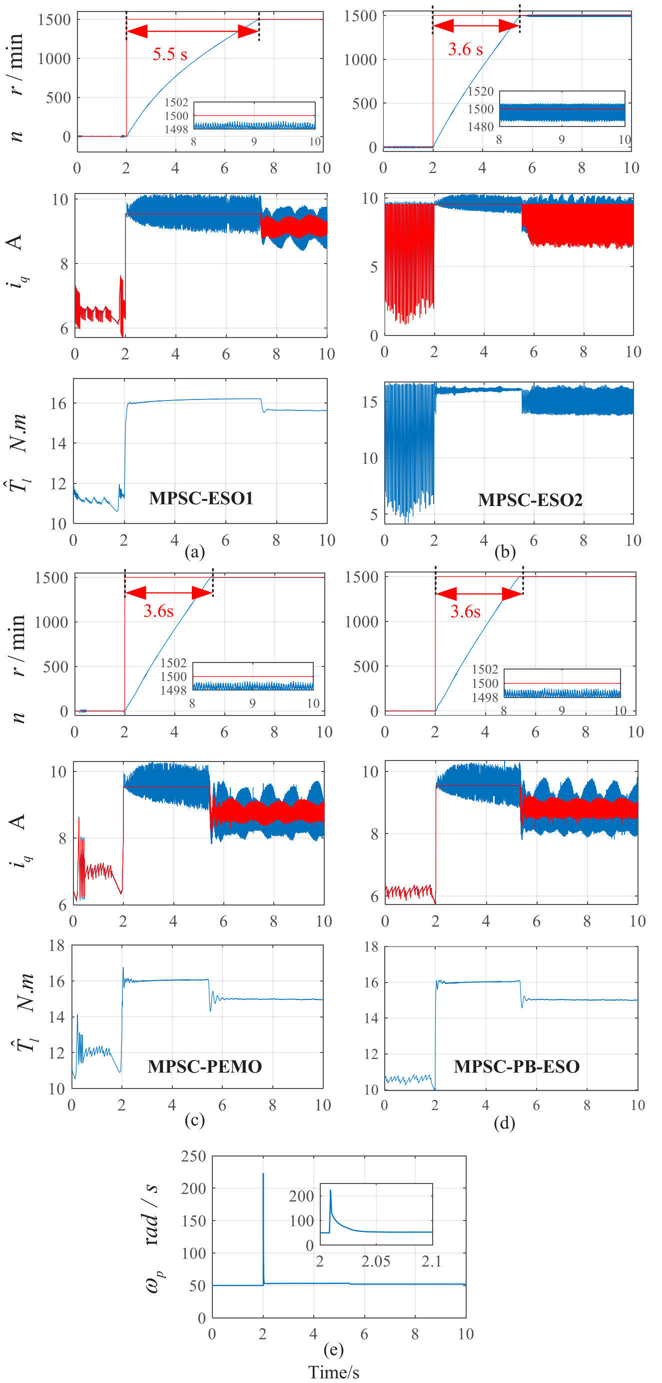

Fig. 7. (Experimental data) The performance of speed from 0 to 1500 r/min under rated load. (a) MPSC-ESO1. (b) MPSC-ESO2. (c) MPSC-PEMO. (d) MPSC-PB-ESO. (e) PB.

TABLE III
COMPUTATIONAL BURDEN OVERVIEW

Parameters	MPSC-ESO	MPSC-PEMO	MPSC-PB-ESO
Execution time	30μs	35μs	35μs
Processor utilization	30%	35%	35%

the MPSC-ESO2 method displays notable current fluctuations. The load disturbance estimation performance in Fig. 7 explains this issue: the high-bandwidth ESO introduces excessive measurement noise into the load disturbance estimation, leading to significant fluctuations in the reference current generated by MPSC-ESO2.

Fig. 7(e) illustrates the dynamic process of the PB ω_p in the MPSC-PB-ESO method. Following the input of the reference signal, the PB rapidly increases and then converges to the base bandwidth of 50 rad/s within 0.1 s. This behavior demonstrates that the proposed method enhances both the dynamic and steady-state performance of the MPSC approach by dynamically adjusting the observer gain through abrupt bandwidth changes.

Compared to the MPSC-PEMO method, the MPSC-PB-ESO method demonstrates smaller overshoot and reduced fluctuation in disturbance estimation. However, due to the relatively stable load disturbance under rated conditions, this advantage is not significantly reflected in speed control performance. The following section will evaluate these methods under specific operating conditions.

B. *Robustness Verification*

Model mismatch and abrupt load introduce step disturbances into the system [see (5)]. To assess the robustness of the proposed method, we first evaluate the performance of the MPSC-PB-ESO method under conditions of inertia mismatch and sudden load changes. In this scenario, the IPMSM operates in speed mode with a reference speed of 700 r/min.

Fig. 8 illustrates the performance of all methods when the inertia experiences a sudden change of $\Delta J = 1/3J$ at 0.2 s. In Fig. 8(a)–(d), the upper section of each subplot shows the speed tracking performance, the middle section displays the q-axis reference current, and the lower section presents the observer speed estimation error.

From Fig. 8(a), it can be observed that MPSC-ESO1 stably tracks the 700 r/min reference with a speed ripple of 1.4 r/min. Following the model mismatch, the speed returns to a steady state after 0.13 s.

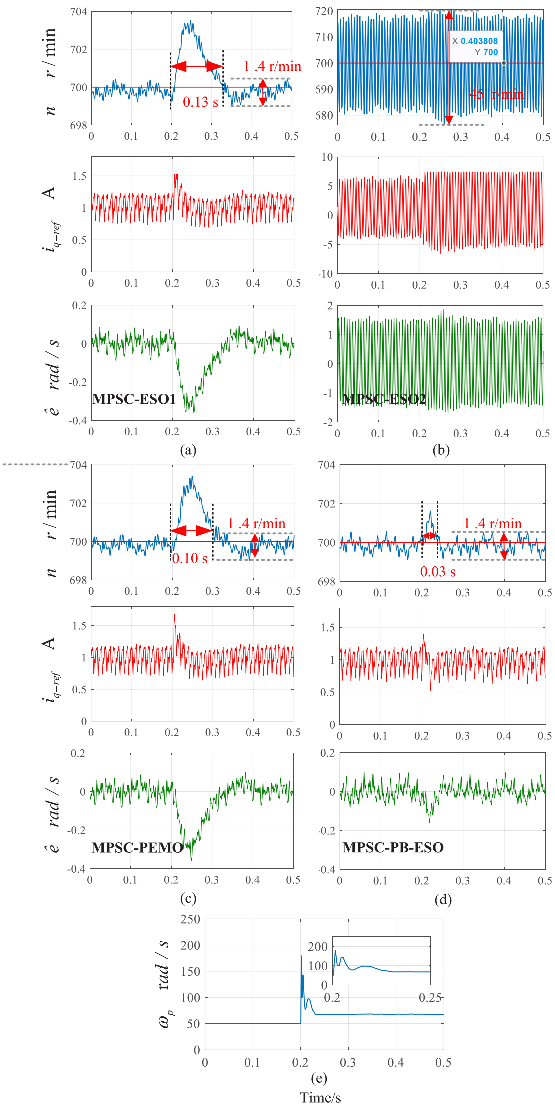

Fig. 8. (Experimental data) The performance of speed tracking when the inertia suddenly changes by $\Delta J = 1/3J$. (a) MPSC-ESO1. (b) MPSC-ESO2. (c) MPSC-PEMO. (d) MPSC-PB-ESO. (e) PB.

Fig. 8(b) illustrates the control performance of MPSC-ESO2, where the motor speed is severely distorted due to the introduction of high-frequency noise. This confirms that higher ESO bandwidth results in increased ripple in the system state. The dynamic performance of MPSC-ESO2 under model mismatch is significantly affected and will not be further discussed.

Fig. 8(c) and (d) shows the performance of MPSC-PEMO and MPSC-PB-ESO, respectively. Like MPSC-ESO1, both methods exhibit a speed ripple amplitude of 1.4 r/min, indicating that neither PEMO nor PB-ESO introduces significant high-frequency measurement noise. In terms of recovery time, MPSC-PEMO requires 0.1 s, while MPSC-PB-ESO recovers in just 0.03 s. These results demonstrate that the proposed method effectively suppresses measurement noise while ensuring a rapid convergence rate under model mismatch conditions.

Fig. 9 illustrates the performance of the MPSC-ESO method under abrupt load conditions. From 0 to 0.2 s, the IPMSM is subjected only to Coulomb and friction torques. At 0.2 s, a sudden load torque of 3.5 N· m is applied.

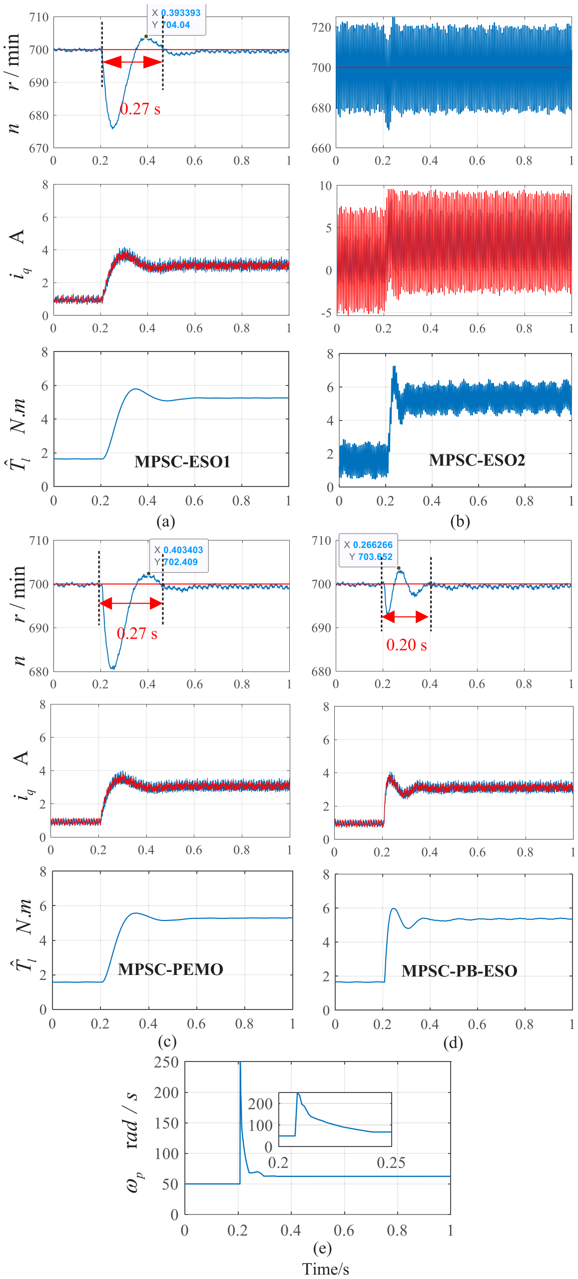

Fig. 9. (Experimental data) The performance of speed tracking under the abrupt load. (a) MPSC-ESO1. (b) MPSC-ESO2. (c) MPSC-PEMO. (d) MPSC-PB-ESO. (e) PB.

In Fig. 9(a)–(d), the upper section of each subplot shows the speed tracking performance, the middle section depicts the q-axis reference current (red line) alongside its measurement value (blue line), and the lower section presents the load observation values.

Similar to the model mismatch scenario, MPSC-ESO1 and MPSC-ESO2 exhibit limitations in both recovery time and ripple reduction. In contrast, MPSC-PB-ESO and MPSC-PEMO demonstrate shorter recovery times while maintaining low ripple. Notably, the proposed method is the fastest, returning to

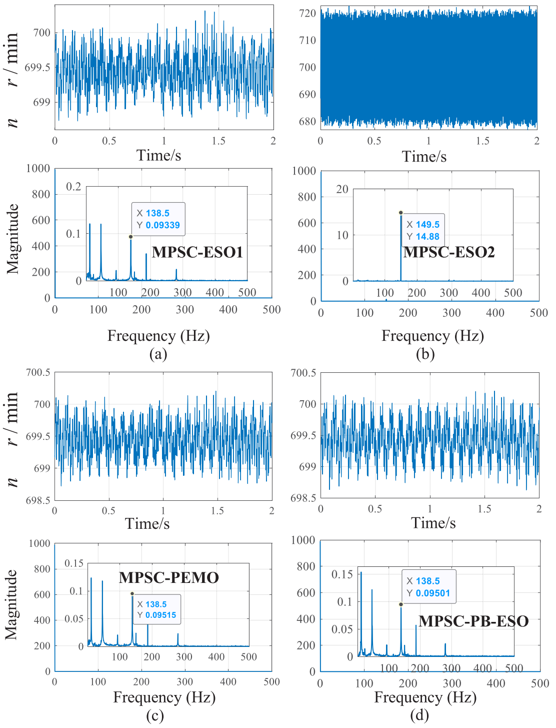

Fig. 10. (Experimental data) FFT of speed signals with a speed of 700 r/min. (a) MPSC-ESO1. (b) MPSC-ESO2. (c) MPSC-PEMO. (d) MPSC-PB-ESO.

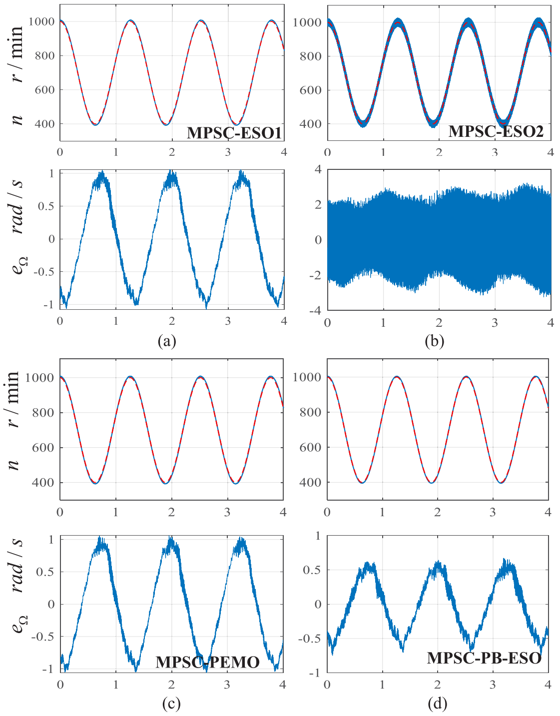

Fig. 11. (Experimental data) The performance of speed tracking under the dynamic reference speed (The red dashed line represents the given speed). (a) MPSC-ESO1. (b) MPSC-ESO2. (c) MPSC-PEMO. (d) MPSC-PB-ESO.

a steady state within just 0.2 s. The q-axis current tracking performance and load observation results further support this conclusion.

Fig. 8(e) and 9(e) illustrate the dynamic behavior of the PB ω_p for PB-ESO. The value of ω_p peaks before the maximum estimation error occurs, exhibiting transient and anticipatory characteristics. This behavior indicates that integrating PB-ESO with MPSC significantly improves speed tracking performance and effectively handles step disturbances in the ED system.

It is important to note that, as derived from Figs. 8(e) and 9(e), a smaller coefficient a in (19) reduces the sensitivity of the PB to unknown disturbances, while a coefficient a that is large makes it difficult for the PB to quickly converge to the basic bandwidth and may introduce additional noise. Therefore, the coefficient a is typically chosen within the range of 1 to 10.

Fig. 10 shows the frequency spectrum characteristics obtained from the fast Fourier analysis (FFT) of the motor speed signal at 700 r/min over a duration of 2 s. From Fig. 10, it can be observed that the maximum amplitudes of high-frequency signal of the proposed method and the MPSC-PEMO method do not exceed 0.1 r/min, which is similar to the MPSC-ESO1 method. In contrast, the maximum amplitudes of high-frequency signal of the MPSC-ESO2 method reached 14.88 r/min, an increase of 148 times. This further explains that the proposed PB-ESO exhibits performance in noise suppression comparable to that of low-bandwidth ESO methods.

C. Dynamic Speed and Dynamic Load Tracking Performance

ED often operates at dynamic speeds and dynamic load conditions, such as in servo systems and electric vehicles. To explore the dynamic performance of the proposed method, MPSC-PB-ESO is experimentally verified under sinusoidal reference speed and sinusoidal load conditions, as shown in Figs. 11 and 12. The red dotted line represents the reference value.

For the dynamic reference speed, a common sine wave speed reference, $300\sin(5t) + 700$ r/min, is adopted. e_Ω is defined as the tracking error of speed. From Fig. 11(d), it can be seen that the MPSC-PBO has the smallest amplitude of tracking error under the dynamic reference (1.3 rad/s). In contrast, the tracking errors of the MPSC-ESO1 and the MPSC-PEMO both reach 2.1 rad/s, which is twice as much as that of the proposed method. The amplitude of ripple for the MPSC-ESO2 is approximately 6 rad/s, the highest among all methods. As mentioned earlier, this is caused by high-frequency measurement noise.

Next, the dynamic load is considered. To test the limiting performance of the proposed method, a sine wave load torque with a frequency of 48 rad/s ($4\sin(48t) + 1.75\,\mathrm{N\cdot m}$) is selected, which is close to the bandwidth $\omega_o = 50$ rad/s. Fig. 12 shows the performance and load of all methods under dynamic load. The upper part of each block displays the speed tracking performance, the middle part shows the load estimation, and the lower part zooms in on the estimated load within 0.2 s.

From the upper part of each block in Fig. 12, it can be seen that the motor speed driven by all methods struggles to maintain the reference speed of 700 r/min and fluctuates sinusoidally with the load changes. In load estimation, the amplitudes of ESO1 and PEMO differ greatly from the actual load, consistent with the theoretical derivation. The maximum error of ESO1 is 1.6 $\mathrm{N\cdot m}$, and that of PEMO is 1.54 $\mathrm{N\cdot m}$. This discrepancy arises

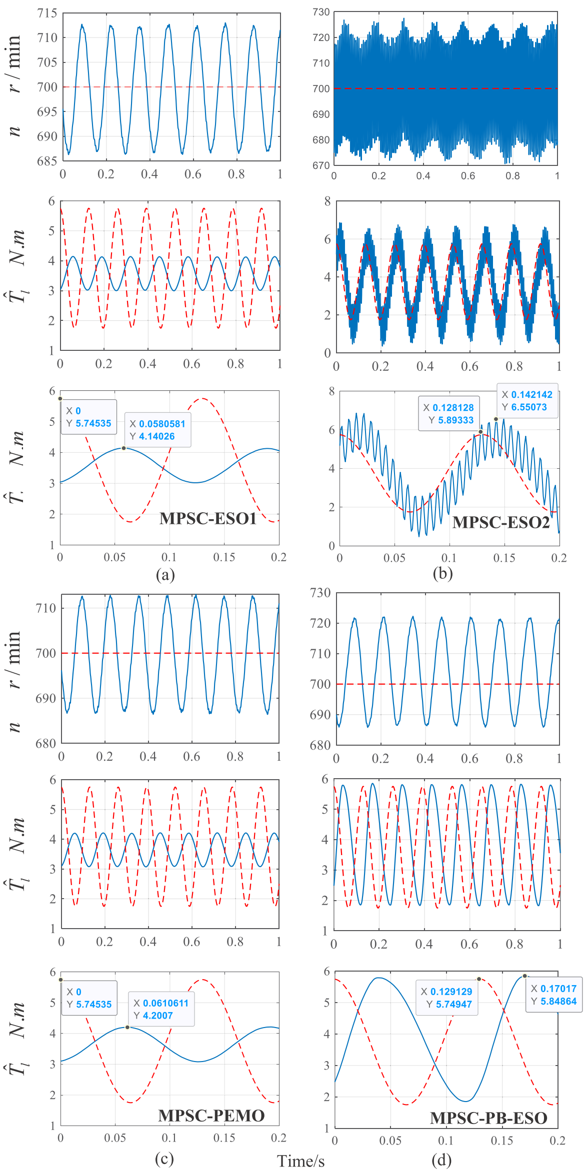

(a) (b) (c) (d)

Fig. 12. (Experimental data) The performance of speed tracking under the dynamic load torque (The red dashed line represents the given speed or actual load). (a) MPSC-ESO1. (b) MPSC-ESO2. (c) MPSC-PEMO. (d) MPSC-PB-ESO.

because the interference estimation mechanisms of ESO and PEMO exhibit a monotonous decrease. For the high-bandwidth ESO, the load estimation deviation of ESO2 is 0.66 N · m, which is still large due to the excessivew ripple.

For the proposed PB-ESO method, the estimated load amplitude and frequency match the actual load, demonstrating excellent tracking performance. This proves the effectiveness of the proposed method. However, the estimated load of all methods shows a large delay for high-frequency loads, which is caused by the group delay of the filter.

D. Comparison Summary

To comprehensively evaluate the proposed method, the key performance indicators for all methods under four operating conditions—namely, speed ripple, recovery time from disturbances, tracking error with dynamic reference speed, and observation error under dynamic load—were extracted and compared. The results are presented in Fig. 13 through circular bar charts. Due to the poor performance of MPSC-ESO2, it was excluded from the final comparative analysis. From Fig. 13, under the step load disturbance, the recovery time of MPSC-PB-ESO is 26% shorter than that of MPSC-ESO1 and MPSC-PEMO. With a dynamic reference, the speed tracking error amplitude of MPSC-PB-ESO is 38% lower than that of the MPSC-ESO1 and MPSC-PEMO. Under the dynamic load conditions, the load estimation error of MPSC-PB-ESO is 94% lower than that of MPSC-ESO1 and 93% smaller than that of MPSC-PEMO. Clearly, the proposed strategy achieves outstanding performance to the CCS-MPSC system.

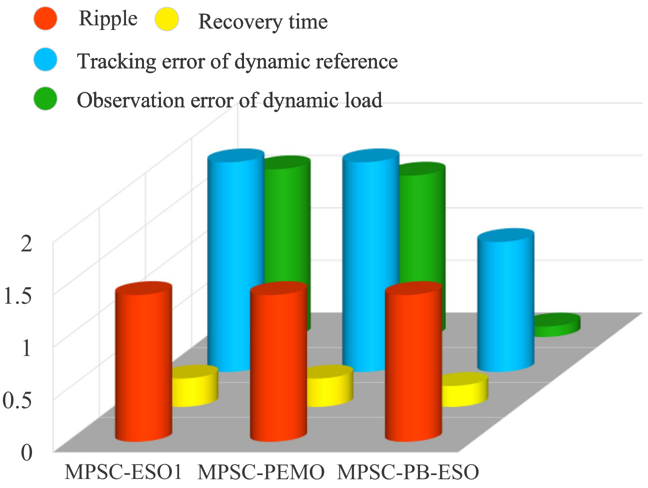

Fig. 13. Overall comparison of three control methods under different conditions.

V. CONCLUSION

This study investigates the utilization of a PB-ESO with gain optimization in CCS-MPSC of ED. The effectiveness of the proposed control method is experimentally validated and compared within a commonly used IPMSM systems in ED.

It should be noted that, despite the amplitude and frequency of the estimated interference by PB-ESO being consistent with the actual interference, a significant time-delay estimation persists for periodic fast time-varying interference. In the future, the gains of PB-ESO should be further improved. Designing the gains of ESO with reference to a zero-delay filter might prove to be more effective.

REFERENCES

[1] S. Ding, Q. Hou, and H. Wang, "Disturbance-observer-based second-order sliding mode controller for speed control of PMSM drives," *IEEE Trans. Energy Convers.*, vol. 38, no. 1, pp. 100–110, Mar. 2023.

[2] T. Yang, Y. Deng, and H. Li, "Fast integral terminal sliding mode control with a novel disturbance observer based on iterative learning for speed control of PMSM," *ISA Trans.*, vol. 134, pp. 460–471, 2023.

[3] R. Grandia, F. Jenelten, S. Yang, F. Farshidian, and M. Hutter, "Perceptive locomotion through nonlinear model-predictive control," *IEEE Trans. Robot.*, vol. 39, no. 5, pp. 3402–3421, Oct. 2023.

[4] T. T. Nguyen, H. N. Tran, T. H. Nguyen, and J. W. Jeon, "Recurrent neural network-based robust adaptive model predictive speed control for PMSM with parameter mismatch," *IEEE Trans. Ind. Electron.*, vol. 70, no. 6, pp. 6219–6228, Jun. 2023.

[5] E. Fuentes, D. Kalise, J. Rodriguez, and R. M. Kennel, "Cascade-free predictive speed control for electrical drives," *IEEE Trans. Ind. Electron.*, vol. 61, no. 5, pp. 2176–2184, May 2014.

[6] X. Liu, J. Wang, X. Gao, W. Tian, L. Zhou, and R. Kennel, "Robust predictive speed control of SPMSM drives with algebraically designed weighting factors," *IEEE Trans. Power Electron.*, vol. 37, no. 12, pp. 14434–14446, Dec. 2022.

[7] X. Zhang, Y. Cheng, Z. Zhao, and Y. He, "Robust model predictive direct speed control for SPMSM drives based on full parameter disturbances and load observer," *IEEE Trans. Power Electron.*, vol. 35, no. 8, pp. 8361–8373, Aug. 2020.

[8] Z. Li, F. Wang, D. Ke, J. Li, and W. Zhang, "Robust continuous model predictive speed and current control for PMSM with adaptive integral sliding-mode approach," *IEEE Trans. Power Electron.*, vol. 36, no. 12, pp. 14398–14408, Dec. 2021.

[9] W.-H. Chen, J. Yang, L. Guo, and S. Li, "Disturbance-observer-based control and related methods—an overview," *IEEE Trans. Ind. Electron.*, vol. 63, no. 2, pp. 1083–1095, Feb. 2016.

[10] H. T. Nguyen and J.-W. Jung, "Disturbance-rejection-based model predictive control: Flexible-mode design with a modulator for three-phase inverters," *IEEE Trans. Ind. Electron.*, vol. 65, no. 4, pp. 2893–2903, Apr. 2018.

[11] E. J. Fuentes, C. A. Silva, and J. I. Yuz, "Predictive speed control of a two-mass system driven by a permanent magnet synchronous motor," *IEEE Trans. Ind. Electron.*, vol. 59, no. 7, pp. 2840–2848, Jul. 2012.

[12] X. Liu et al., "Continuous control set predictive speed control of SPMSM drives with short prediction horizon," *IEEE Trans. Power Electron.*, vol. 37, no. 9, pp. 10166–10177, Sep. 2022.

[13] Y. Xu, Y. Hou, and Z. Li, "Robust predictive speed control for SPMSM drives based on extended state observers," *J. Power Electron.*, vol. 19, no. 2, pp. 497–508, 2019.

[14] Y. Zhang, J. Jin, and L. Huang, "Model-free predictive current control of PMSM drives based on extended state observer using ultralocal model," *IEEE Trans. Ind. Electron.*, vol. 68, no. 2, pp. 993–1003, Feb. 2021.

[15] Z. Sun, Y. Deng, J. Wang, H. Li, and H. Cao, "Improved cascaded model-free predictive speed control for PMSM speed ripple minimization based on ultra-local model," *ISA Trans.*, vol. 143, pp. 666–677, 2023.

[16] S. Gao, Y. Wei, D. Zhang, H. Qi, Y. Wei, and Z. Yang, "Model-free hybrid parallel predictive speed control based on ultralocal model of PMSM for electric vehicles," *IEEE Trans. Ind. Electron.*, vol. 69, no. 10, pp. 9739–9748, Oct. 2022.

[17] F. Wang, D. Ke, X. Yu, and D. Huang, "Enhanced predictive model based deadbeat control for PMSM drives using exponential extended state observer," *IEEE Trans. Ind. Electron.*, vol. 69, no. 3, pp. 2357–2369, Mar. 2022.

[18] Z. Song, F. Zhou, and Z. Zhang, "Parallel-observer-based predictive current control of permanent magnet synchronous machines with reduced switching frequency," *IEEE Trans. Ind. Inform.*, vol. 15, no. 12, pp. 6457–6467, Dec. 2019.

[19] J. Wang, Y. Liu, J. Yang, F. Wang, and J. Rodríguez, "Adaptive integral extended state observer based improved multi-step FCS-MPCC for PMSM," *IEEE Trans. Power Electron.*, vol. 38, no. 9, pp. 11260–11276, Sep. 2023.

[20] F. Wang and L. He, "FPGA-based predictive speed control for PMSM system using integral sliding-mode disturbance observer," *IEEE Trans. Ind. Electron.*, vol. 68, no. 2, pp. 972–981, Feb. 2021.

[21] S. Li, Y. Xu, W. Zhang, and J. Zou, "Robust deadbeat predictive direct speed control for PMSM with dual second-order sliding-mode disturbance observers and sensitivity analysis," *IEEE Trans. Power Electron.*, vol. 38, no. 7, pp. 8310–8326, Jul. 2023.

[22] D. Ke, F. Wang, X. Yu, S. A. Davari, and R. Kennel, "Predictive error model based enhanced observer for PMSM deadbeat control systems," *IEEE Trans. Ind. Electron.*, vol. 71, no. 3, pp. 2242–2252, Mar. 2024.

[23] J. Li, L. Zhang, S. Li, and J. Su, "A time delay estimation interpretation of extended state observer-based controller with application to structural vibration suppression," *IEEE Trans. Autom. Sci. Eng.*, vol. 21, no. 2, pp. 1965–1973, Apr. 2024.

[24] T. Zhang, Z. Xu, and C. Gerada, "A nonlinear extended state observer for sensorless IPMSM drives with optimized gains," *IEEE Trans. Ind. Appl.*, vol. 56, no. 2, pp. 1485–1494, Mar./Apr. 2020.

[25] Y. Zuo, J. Mei, X. Zhang, and C. H. Lee, "Simultaneous identification of multiple mechanical parameters in a servo drive system using only one speed," *IEEE Trans. Power Electron.*, vol. 36, no. 1, pp. 716–726, Jan. 2021.

[26] Y. Chen, M. Yang, J. Long, W. Qu, D. Xu, and F. Blaabjerg, "A moderate online servo controller parameter self-tuning method via variable-period inertia identification," *IEEE Trans. Power Electron.*, vol. 34, no. 12, pp. 12165–12180, Dec. 2019.

[27] S. Kim, "Moment of inertia and friction torque coefficient identification in a servo drive system," *IEEE Trans. Ind. Electron.*, vol. 66, no. 1, pp. 60–70, Jan. 2019.

[28] K. Liu, C. Hou, and W. Hua, "A novel inertia identification method and its application in pi controllers of PMSM drives," *IEEE Access*, vol. 7, pp. 13445–13454, 2019.

[29] T. Wang, G. Luo, Z. Chen, W. Tu, and C. Liu, "An improved robust model predictive speed control with inertia identification for PMSM drives in electro-hydrostatic actuator," *IEEE Trans. Power Electron.*, vol. 38, no. 11, pp. 13825–13841, Nov. 2023.

[30] Z. Pu, R. Yuan, J. Yi, and X. Tan, "A class of adaptive extended state observers for nonlinear disturbed systems," *IEEE Trans. Ind. Electron.*, vol. 62, no. 9, pp. 5858–5869, Sep. 2015.

[31] Y. Du, W. Cao, and J. She, "Analysis and design of active disturbance rejection control with an improved extended state observer for systems with measurement noise," *IEEE Trans. Ind. Electron.*, vol. 70, no. 1, pp. 855–865, Jan. 2023.

[32] F. Tinazzi, P. G. Carlet, S. Bolognani, and M. Zigliotto, "Motor parameter-free predictive current control of synchronous motors by recursive least-square self-commissioning model," *IEEE Trans. Ind. Electron.*, vol. 67, no. 11, pp. 9093–9100, Nov. 2020.

[33] L. Harnefors and H.-P. Nee, "Model-based current control of AC machines using the internal model control method," *IEEE Trans. Ind. Appl.*, vol. 34, no. 1, pp. 133–141, Jan./Feb. 1998.